Materials Advances

ROYAL SOCIETY OF CHEMISTRY

PAPER

View Article Online
View Journal | View Issue

Cite this: *Mater. Adv.*, 2021, 2, 7773

Indoor light-harvesting dye-sensitized solar cells surpassing 30% efficiency without co-sensitizers†

Reethu Haridas,‡[ab] Jayadev Velore,‡[ab] Sourava Chandra Pradhan,[ab] Asarikal Vindhyasarumi,[a] Karuvath Yoosaf, *[ab] Suraj Soman, *[ab] K. N. Narayanan Unni *[ab] and Ayyappanpillai Ajayaghosh *[ab]

Received 9th September 2021,
Accepted 5th October 2021

DOI: 10.1039/d1ma00829c

rsc.li/materials-advances

Dye-sensitized solar cells (DSCs) have proven to be one of the best photovoltaic approaches for harnessing indoor/artificial light. Herein, we report two new molecularly engineered, cost-effective, metal-free, carbazole-based D–π–A sensitizers (**YK 8** and **YK 9**) by judiciously varying their π-spacers, which are suitable for indoor photovoltaic applications. Using **YK 8**, we achieved an efficiency of 28.7% under standard 1000 lux Osram 14 W T2 cool day light fluorescent tube illumination with a power output of 68.88 μW cm^{-2} and 30.24% with a power output of 108.85 μW cm^{-2} under a higher illumination intensity of 1500 lux without co-sensitizers using iodide/triiodide electrolyte. With a small footprint/active area of 1.24 cm^2, we could power a temperature sensor completely autonomously at a low light intensity of 500 lux, displaying the potential of these indoor photovoltaic devices to serve as energy sources for low-power sensors and actuators on the Internet of Things (IoT) network, reducing the dependence on batteries and leading to a smaller carbon footprint. The role of the π-spacer and its influence on recombination and device performance were explored *via* extensive interfacial studies.

1. Introduction

During the past decade, the energy demand and environmental issues associated with the overexploitation of fossil fuels have led to the quest for alternative renewable energy sources. Harnessing solar energy occupies a prominent position as it offers a greener and sustainable way of meeting the energy needs of modern society with a low environmental impact.[1–3] With the emergence of the fourth industrial revolution (Industry 4.0), there is rapid growth (billions) in the application of remote sensors, actuators, and communication devices under the IoT ecosystem powered by batteries, which in turn limits the large-scale deployment of IoT.[4,5] The use of batteries involves significant constraints due to their limited life-span, added operational and maintenance costs, and especially the environmental issues resulting from used batteries.[6,7] These problems have triggered the development of indoor photovoltaics (IPVs).[7–10] IPVs are devices that are capable of harvesting artificial light in indoor space and converting it to useful power, which can be used to transform conventional IoT power nodes into energy-independent self-powered systems.[11–19] Among the various photovoltaic technologies, dye-sensitized solar cells (DSCs) have emerged as one of the leading candidates for power generation under indoor light conditions.[20–23] Their simple design, cost-effectiveness, and ability to maintain high photovoltages in indoor/artificial light conditions make DSCs stand out among IPVs. Using conventional iodide/triiodide electrolyte with organic anthracene-based sensitizers, Tingare *et al.* achieved a PCE of 24.43% under 1200 lux and 28.56% under 6000 lux, which is the best-reported performance under indoor light conditions to date.[24] In 2017, Freitag *et al.* demonstrated the capability of DSCs in artificial lighting environments with a power conversion efficiency of 28.9% under 1000 lux CFL using copper electrolyte.[25] This was followed by contributions from Michael Grätzel and Anders Hagfeldt, proving this to be superior technology among the existing first- and second-generation photovoltaics for indoor light-harvesting applications. They realized an efficiency of 32% (1000 lux CFL) with copper electrolyte, opening new avenues to commercialise this technology.[22] Grätzel and co-workers also achieved an efficiency of 28.4% under 1000 lux fluorescent light tube illumination using an organic dye with the same copper electrolyte.[26] Recent reports have recorded efficiencies greater than 34% with the co-sensitization of organic dyes together with copper electrolyte.[21,27]

[a] *Photosciences and Photonics Section, Chemical Sciences and Technology Division, CSIR-National Institute for Interdisciplinary Science and Technology (CSIR-NIIST), Thiruvananthapuram 695019, India. E-mail: suraj@niist.res.in, ajayaghosh@niist.res.in*

[b] *Academy of Scientific and Innovative Research (AcSIR), Ghaziabad-201002, India*

† Electronic supplementary information (ESI) available. See DOI: 10.1039/d1ma00829c

‡ These authors contributed equally to this work.

In DSCs, dyes/sensitizers occupy a prominent place in determining the PCE by converting incident light to electricity.[8,28–37] With the present advancements in IPV, precisely engineered sensitizers having a good spectral match with indoor/artificial lights (LED/CFL) are prerequisites to achieve improved PCE under indoor/artificial light conditions. Although the conventional ruthenium (Ru) sensitizers have been proven to be the best candidates for sunlight harvesting, they are not suitable for power generation under indoor light. Additionally, the high cost, toxicity, scarcity and low flexibility to impart structural variation limit the use of these metal complexes in IPV. Thus, metal-free organic dyes were introduced to replace metal complex sensitizers by virtue of their low cost and better molecular design possibilities. In general, metal-free organic dyes adopt the donor–π bridge–acceptor (D–π–A) design, enabling superior charge separation, high molar extinction coefficient, easy bandgap engineering and good photostability.[38–41] Diphenylamines, triarylamines, carbazoles, porphyrins and indoles have been used as potential organic sensitizers, among which carbazoles occupy a prominent position due to their high electron-donating capability and improved photo and thermal stability.[29,35,36,39,42–53] DSCs fabricated with one of the well-studied commercial and efficient carbazole dye **MK 2**, having regioregular *n*-hexyl-substituted quarter-thiophene and cyanoacrylic acid resulted in 8.3% power conversion efficiency under 1 sun condition.[54] Later, Kakiage and co-workers demonstrated ~14.5% efficiency employing **MK 2** together with a cocktail mixture of metal-free sensitizers.[42] In this context, we designed and synthesized two carbazole dyes with variable π-spacers (**YK 8** and **YK 9**). The **YK 8** sensitizer is endowed with bis-octyl chains on a terthiophene core to reduce its aggregation and prevent carrier recombination, whereas the **YK 9** dye was designed and synthesized using a more planar thienothiophene linker for better donor–acceptor interactions, facilitating rapid electron migration from the donor to acceptor. Our motivation was to introduce a simple D–π–A sensitizer capable of delivering >30% efficiency under fluorescent tube illumination in a cell structure without co-sensitizers using the conventional iodide/triiodide electrolyte.

2. Results and discussion

2.1. Synthesis of dyes

The dyes used herein possess the general architecture of D–π–A (Fig. 1a). The **YK 8** and **YK 9** dyes consist of *N*-methylcarbazole as the donor and cyanoacrylic acid as the acceptor and anchoring moiety. Structurally, **YK 8** and **YK 9** differ mainly in terms of the π-bridge, wherein the former contains bis-octyl-substituted terthiophene and the latter has a thienothiophene linked to one octyl-substituted thiophene unit. The synthetic strategy adopted for the preparation of **YK 8** and **YK 9** is presented in Fig. 2. Both dyes were obtained in 5–6 steps in good yields (Fig. 2), which promise their cost-effective large-scale production. To prepare **YK 8**, initially Stille coupling reaction of 2,5-bis(tributylstannyl)thiophene with 2-bromo-3-octylthiophene was performed to yield dioctyl-2,2′:5′,2″-terthiophene (**1**), which was then converted to **3** through

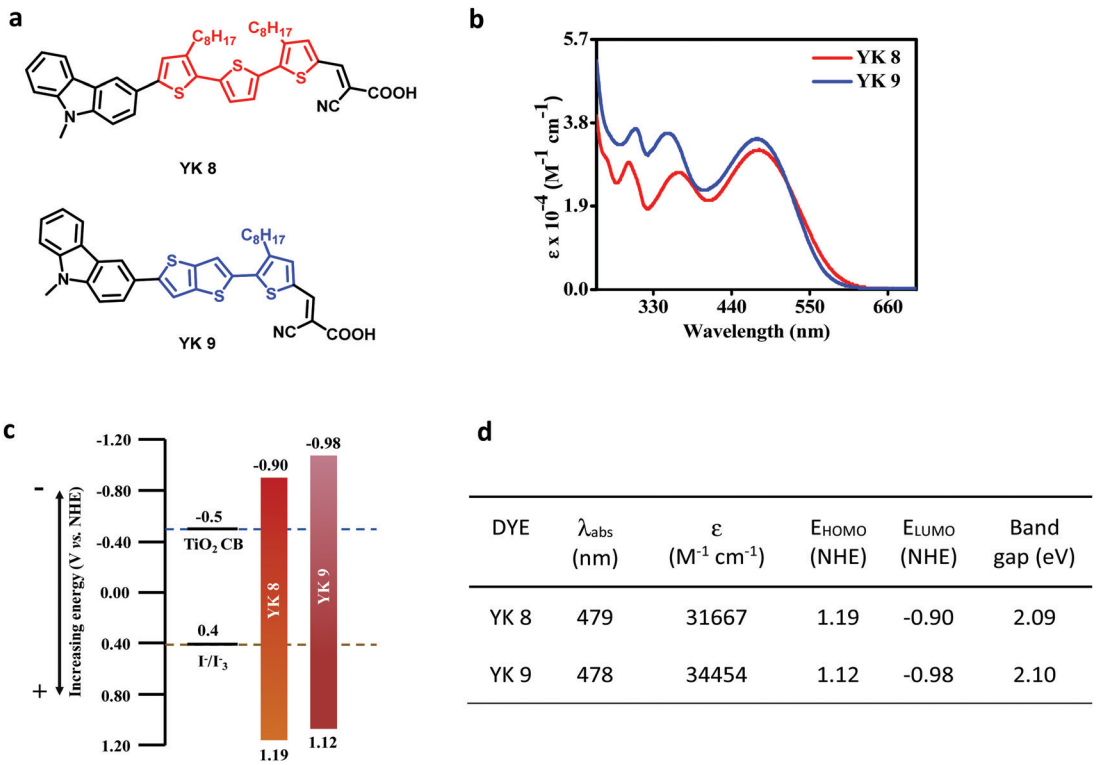

DYE	λ_{abs} (nm)	ε (M^{-1} cm^{-1})	E_{HOMO} (NHE)	E_{LUMO} (NHE)	Band gap (eV)
YK 8	479	31667	1.19	-0.90	2.09
YK 9	478	34454	1.12	-0.98	2.10

Fig. 1 (a) Structure of the **YK 8** and **YK 9** dyes. (b) Absorption spectra of the **YK 8** and **YK 9** dyes in dichloromethane. (c) Energy level diagram of the **YK 8** and **YK 9** dyes illustrating the position of the HOMO with respect to the redox potential of the I^-/I_3^- electrolyte and LUMO with respect to the TiO_2 conduction band. (d) Optical and electrochemical parameters of the **YK 8** and **YK 9** dyes.

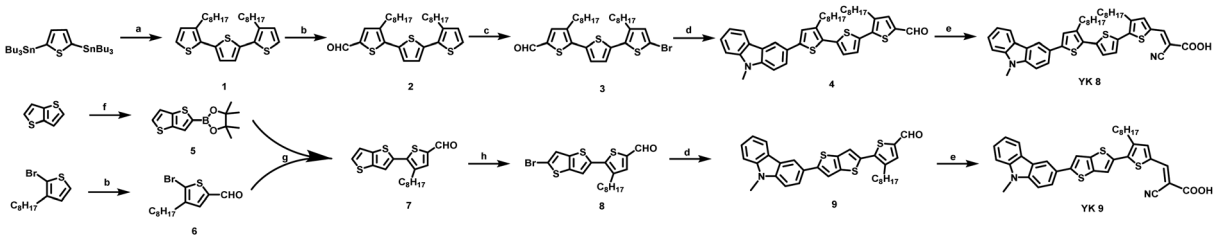

Fig. 2 Synthetic pathway for the **YK 8** and **YK 9** dyes (a) toluene, P(*o*-tolyl)$_3$, $Pd_2(dba)_3$, and 2-bromo-3-octylthiophene, (b) DCE, DMF, and $POCl_3$, (c) DMF and NBS, (d) toluene, 9-methyl-9*H*-carbazole-3-boronic acid pinacol ester, K_2CO_3, and $Pd(PPh_3)_4$, (e) $CHCl_3$, cyanoacetic acid, piperidine, (f) THF, *n*-BuLi, and 2-isopropoxy-4,4,5,5-tetramethyl-4,3,2-dioxaboralane, (g) toluene, K_2CO_3, and $Pd(PPh_3)_4$, and (h) chloroform:acetic acid and NBS.

the Vilsmeier formylation reaction and bromination with NBS. Compound **3** was then converted to **YK 8** through successive Suzuki coupling with 9-methyl-9*H*-carbazole-3-boronic acid pinacol ester and condensation reaction with cyanoacetic acid. Conversely, for the preparation of **YK 9**, intermediates **5** and **6** were prepared separately and coupled *via* Suzuki reaction to yield the first compound **7**, which was subsequently brominated to produce **8**. Similar to **YK 8**, **YK 9** was obtained from **8** through successive Suzuki coupling with 9-methyl-9*H*-carbazole-3-boronic acid pinacol ester and condensation reaction with cyanoacetic acid.

2.2. Optical and electrochemical properties

As expected, the variation in π-architecture did not have any profound effect on the spectral profiles of the dyes. Both dyes exhibited broad absorption in the range of 250–600 nm with three distinguishable peaks (Fig. 1b). The lower energy absorption is mainly due to the intramolecular charge transfer transitions, whereas the two higher energy peaks arise predominantly from the π–π* transition. It should be noted that **YK 9** exhibited a slightly higher molar extinction coefficient (ε@478 nm ≈ 3.4 × 10^4 M^{-1} cm^{-1}) than **YK 8** (ε@479 nm ≈ 3.2 × 10^4 M^{-1} cm^{-1}) in the blue region. Also, **YK 8** showed a slightly red-shifted absorbance and higher molar extinction coefficient in the red region above 500 nm. To ensure effective electron transfer from the dye to the semiconductor and the regeneration of the dyes by the electrolyte, it is important to determine the ground and excited state energy levels of the sensitizers used in DSCs. Hence, we examined the oxidation potentials of the **YK 8** and **YK 9** dye molecules using cyclic voltammetry techniques (linear cyclic voltammetry and square wave voltammetry) in dichloromethane solvent with tetrabutylammonium hexafluorophosphate ($(n\text{-Bu})_4NPF_6$) as the supporting electrolyte, glassy carbon as working electrode, Pt as the counter electrode and Ag/AgCl as the reference electrode. The reference electrode was calibrated using ferrocene as the standard. The cyclic voltammograms and the energy level calculations are provided in Fig. S1(a–c) (ESI†). Although both dyes exhibited quite similar band gaps (~2.1 eV), the HOMO and LUMO energy levels of **YK 9** are positioned slightly above that of **YK 8** (Fig. 1c and d), respectively. In any case, the LUMO levels are located 400 mV above the conduction band of TiO_2, which favourably supports electron injection from the dye excited state upon light absorption. Similarly, the positive shift of dye HOMO levels compared to the I^-/I_3^- redox couple ensures efficient regeneration of the ground state for both dyes.

2.3. Theoretical studies

To gain insight into the electron density distribution in the ground and excited states of the YK dyes, we performed molecular modelling experiments. To reduce the complexity in modelling, the octyl chains present in the π-bridge were replaced with methyl groups, given that this operation would not cause considerable changes to the optoelectronic properties of the light-harvesting core. The geometries were first optimized in the gas phase using the DFT method at the B3LYP/6-311G(d,p) level in the Gaussian 16 program package.[55,56] The optimized structure of the dyes and the electron density delocalization in their HOMO and LUMO energy levels are depicted

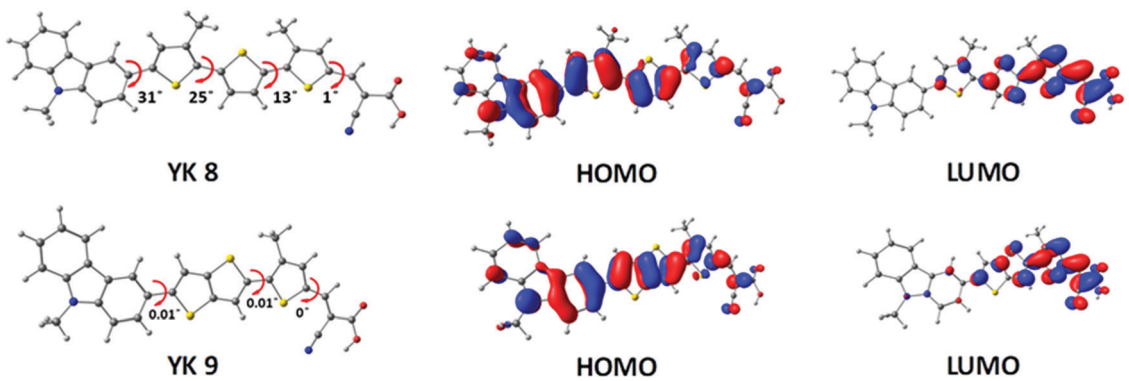

Fig. 3 Optimized geometry, ground state and excited state electron density distribution for the **YK 8** and **YK 9** dyes.

in Fig. 3. Compared to **YK 8**, **YK 9** exhibits a planar π-backbone, leading to more dye loading and aggregation. In both cases, the electron density of the HOMO is distributed all over the dyes and extended towards the thiophene π-spacer, including the anchoring group, whereas for the LUMO, the electron density is primarily localized on the cyanoacrylic acid and adjacent thiophene units.

The **MK 2** sensitizer also shows a similar HOMO electron density distribution, where the HOMO is delocalized over the whole **MK 2** molecule, including the anchoring group, as reported previously.[57,58] Despite having similar HOMO electron density distributions, the **YK 8** and **YK 9** sensitizers showed a difference in recombination given that it depends on factors such as number of alkyl chains, orientation of the dye molecules, Fermi–Dirac distribution of electrons in the TiO_2 conduction band and aggregation. Recently H. Zhang *et al.* has also reported that a small proportion of the HOMO distributed on the anchoring groups of dyes could also reduce charge recombination.[59] The HOMO, LUMO and band gap values obtained from the theoretical studies are presented in Table 1, which agree well with the experimental results. We also calculated the light-harvesting efficiency (LHE) of the dyes *via* TDDFT calculations in toluene (PCM) based on the 6-311G(d,p) basis sets with M062X functional using the equation LHE = $1–10^{-f}$, where f is the oscillator strength obtained from TDDFT calculations and the estimated LHE of the two dyes are 0.97 and 0.98 for **YK 8** and **YK 9**, respectively. The energy transfer percentage from the HOMO to LUMO is 61% and 64% for the **YK 8** and **YK 9** sensitizers, respectively.

2.4. Photovoltaic performance

Dye-sensitized solar cells were fabricated using the conventional architecture, as reported previously by our group, which is provided in Fig. S2a (ESI†). The detailed fabrication procedures are given in the Experimental section, and the fabricated devices are shown in Fig. S2b (ESI†). Details on the certified equipment used for characterization are also provided in the ESI.† The current density–voltage (J–V) characteristics were measured under one sun illumination (100 mW cm^{-2}, AM1.5G). To achieve better power conversion efficiency, we carried out detailed optimization of the semiconductor architecture and co-adsorbent concentration for both the **YK 8** and **YK 9** dyes. The J–V plots are displayed in Fig. S3 and S4 (ESI†), and the tabulated data is summarized in Table S1 and S2 (ESI†). Initial optimization of the TiO_2 layer thickness was carried out without a co-adsorbent (CDCA), where the **YK 8**-based DSCs exhibited a power conversion efficiency of 6.62% ± 0.04% using 6 μm TiO_2 and 6.30% ± 0.02% using 10 μm TiO_2. **YK 9** exhibited a power conversion efficiency of 6.55% ± 0.21% with a 6 μm TiO_2 layer and 5.51% ± 0.02% using a 10 μm TiO_2 layer. With the added advantage of having a higher molar extinction coefficient in the visible region, both organic metal-free sensitizers exhibited the best performances with a 6 μm TiO_2 layer. Thinner electrodes render better transparencies and also contribute to less dye usage, thereby reducing the production cost.

One of the significant problems associated with organic metal-free sensitizers is the aggregation of the dyes on the semiconductor surface. Thus, to control the dye aggregation, leading to a higher performance, we carried out a co-adsorbent concentration-dependent study by varying the concentration of chenodeoxycholic acid. **YK 8** delivered the best power conversion efficiency of 7.49% ± 0.09% for the devices fabricated with 1 mM CDCA, whereas **YK 9** exhibited the best PCE of 6.60% ± 0.13% using 5 mM CDCA (Table 2). The results obtained for the detailed optimization involving various CDCA concentrations (0 mM, 1 mM, 2.5 mM, 5 mM and 10 mM) are summarized in Fig. S4 and Table S2 (ESI†). These observations indicate that **YK 9** is more prone to aggregation on the surface of TiO_2. The **YK 9** dye has only one alkyl chain grafted to the thiophene π-spacer compared to **YK 8**, which has two-alkyl chains attached to the π-spacer. The presence of alkyl chains prevents the aggregation of the **YK 8** dye on the semiconductor surface at the expense of the number of dye molecules. The adsorbed amount of dye molecules for **YK 8** and **YK 9** is 9.76×10^{-8} mol cm^{-2} and 18.08×10^{-8} mol cm^{-2}, respectively. Additionally, the incorporation of a more planar thienothiophene π-spacer in **YK 9** dye contributed to its planar geometry, as evident from its dihedral angle (Fig. 3). This better planarity led to stronger π–π interactions, resulting in more aggregation and leading to higher charge recombination and decreased performance for **YK 9** compared to **YK 8**. It is evident that the much higher amount of surface coverage of **YK 9** is just more aggregates and detrimental to the solar cell performance. Thus, the surface coverage of **YK 8** is enough for efficient light-harvesting, as can be inferred from the absorption spectrum of the dyes on TiO_2 and the IPCE spectra. The UV-Vis spectra of the dye-adsorbed TiO_2 film (Fig. S5, ESI†) show that both the **YK 8** and **YK 9** sensitized photoanodes show strong absorption bands in the visible region (300–680 nm), and **YK 8** shows a red-shifted absorption in the longer wavelength region compared with **YK 9**, similar to the IPCE plot (Fig. 4b).

For both the **YK 8** and **YK 9** dyes, their photovoltaic performance improved with time (ageing). Initially, **YK 8** and **YK 9** exhibited a power conversion efficiency of 7.49% ± 0.09% and 6.90% ± 0.10%, which improved to 9.39% ± 0.18% and 7.48% ± 0.03% with the ageing of the devices under standard indoor conditions for close to four months (2700 h), respectively

Table 1 Electrochemical parameters of **YK 8** and **YK 9** dyes obtained from the theoretical method

Dye	HOMO (eV)	LUMO (eV)	Bandgap (eV)
YK 8	−5.38	−2.99	2.38
YK 9	−5.42	−3.02	2.40

Table 2 Summary of photovoltaic performance of DSCs based on the **YK 8** and **YK 9** dyes

Device	V_{oc} (mV)	J_{sc} (mA cm^{-2})	Integrated J_{sc} (mA cm^{-2})	FF (%)	Efficiency (%)
YK 8	688 ± 4	16.20 ± 0.13	15.84	67.10 ± 0.18	7.49 ± 0.09
YK 9	697 ± 2	13.82 ± 0.08	13.04	68.29 ± 0.27	6.60 ± 0.13

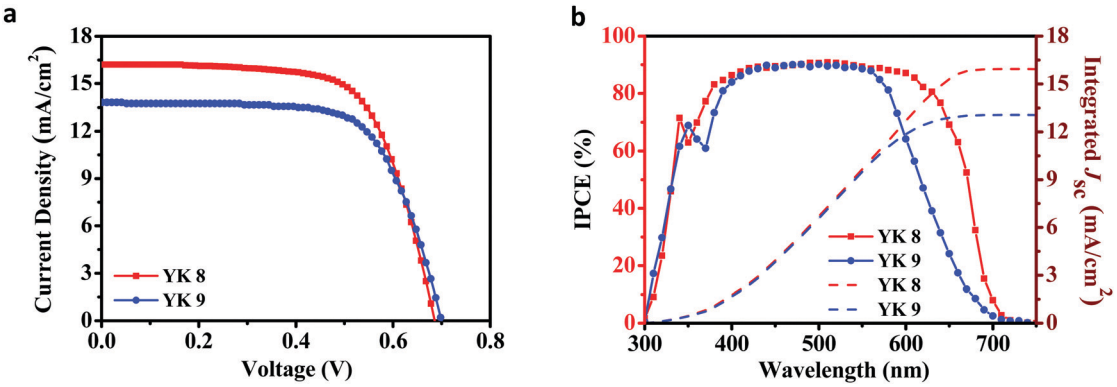

Fig. 4 (a) Current density–voltage (*J*–*V*) characteristics and (b) incident photon-to-current conversion efficiency (*IPCE*) and integrated J_{sc} calculated from IPCE spectra for DSCs fabricated using the **YK 8** and **YK 9** dyes.

(Fig. S6 and Table S4, ESI†). **YK 8** showed a 25.37% increase in PCE with ageing, whereas **YK 9** exhibited around an 8.40% increase in PCE. With the best-optimized device architecture and co-adsorbent concentration, the power conversion efficiency of 9.39% ± 0.18% with J_{sc} of 17.24 ± 0.10 mA cm^{-2}, V_{oc} of 790 ± 6 mV and FF of 68.93 ± 0.29% were achieved for the **YK 8** dye under one sun illumination (100 mW cm^{-2}, AM1.5G) after 2700 h. Similarly, **YK 9** exhibited a PCE of 7.48% ± 0.03% with a J_{sc} of 14.26 ± 0.02 mA cm^{-2}, V_{oc} of 750 ± 1 mV and FF of 69.91% ± 0.35% after 2700 h. We used the commercially available standard carbazole-based metal free organic dye **MK 2** to benchmark and compare the photovoltaic performance of our newly synthesized sensitizers. Under similar experimental conditions, **MK 2** exhibited a PCE of 7.74% ± 0.04% with a J_{sc} of 15.11 ± 0.07 mA cm^{-2}, V_{oc} of 751 ± 1 mV and FF of 68.26% ± 0.15% (Fig. S7 and Table S3, ESI†). Fig. 5(d) shows the variations in efficiency as a function of time, where both the **YK 8** and **YK 9** dyes outperformed the commercial **MK 2** dye and exhibited their best performance after remaining in the dark for 2700 h (~4 months). The enhancement in PV

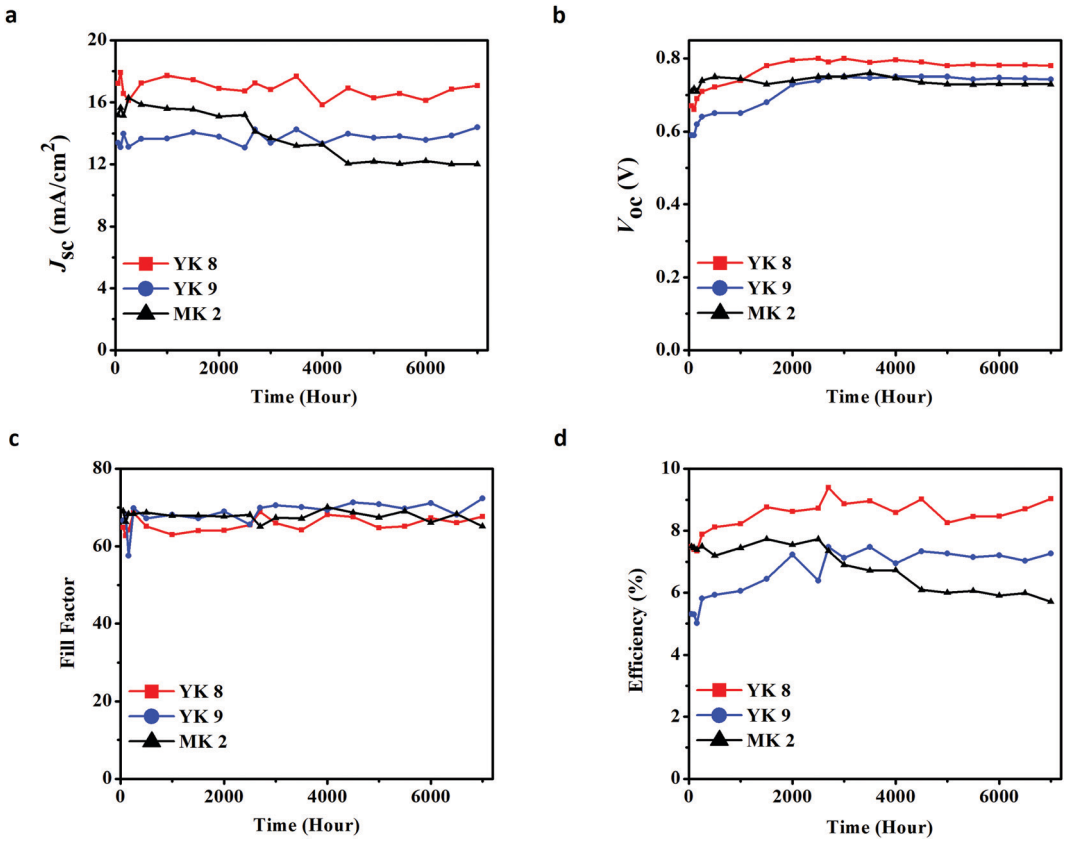

Fig. 5 (a) J_{sc} *versus* time, (b) V_{oc} *versus* time, (c) fill factor *versus* time, and (d) efficiency *versus* time up to 7000 h for DSCs using **YK 8**, **YK 9** and **MK 2** sensitizers.

performance with ageing can be attributed to the better pore filling and electrolyte infiltration in the semiconductor matrix, leading to better dye regeneration and charge collection, as reported previously.[60] These factors contribute to the variation in PCE with ageing for both dyes. The use of a thin-film photoanode contributed to a decrease in the density of band-gap trap states (DOS) and the surface area of the semiconductor, which may have contributed to a better electron lifetime (τ_n), electron diffusion length (L_n) and charge collection efficiency (η_{cc}).[61,62] This is reflected in the IPCE spectra of both dyes after ageing with over 90% absorption in the visible region (Fig. S6b, ESI†). To avoid the overestimation of J_{sc} due to stray light, during all the photovoltaic characterizations, we used a black mask with an aperture of 0.1256 cm^2 (radius of 2 mm) over the device with a total active area of 0.31 cm^2. All the photovoltaic results reported are from the data obtained from 8 devices, and the error was estimated using the standard deviation method. We integrated J_{sc} from the IPCE measurement, which falls well within the permissible error limits with the J_{sc} obtained from the IV measurements [mismatch is only 2.22% for **YK 8** and 5.64% for **YK 9** (for the fresh devices) and 1.3% for **YK 8** and 3.8% for **YK 9** (for the aged devices, 2700 h)], measured under standard experimental conditions. It is clear from Fig. 4b that there is a red-shift in the IPCE spectra for the **YK 8** dye between 550 nm and 700 nm compared to **YK 9**, which contributed to an extra 3 mA cm^{-2} current density for the **YK 8** dye. The IPCE values in the blue region and the onset of IPCE for both **YK 8** and **YK 9** are the same.

Ensuring device stability is the prime pre-requisite for potential sensitizers to be developed from small-area cells to large-area modules. Fig. 5 reveals 7000 h of stability measurements carried out by keeping the devices under standard indoor conditions and carrying out the measurements at 500 h intervals for the **YK 8**, **YK 9** and commercial **MK 2** dyes. **YK 8** showed $<1\%$ decrease in V_{oc}, $\sim5\%$ decrease in J_{sc}, $\sim6\%$ decrease in FF and $\sim12\%$ decrease in overall efficiency after 7000 h. Likewise, **YK 9** showed a nearly constant V_{oc}, $\sim3\%$ decrease in J_{sc}, $<1\%$ decrease in FF and $\sim2\%$ drop in efficiency after 7000 h. In contrast, the commercial **MK 2** dye resulted in an $\sim3\%$ decrease in V_{oc}, $\sim19\%$ decrease in J_{sc}, and $\sim2\%$ decrease in FF, which contributed to a $>20\%$ decrease in efficiency after 7000 h. These results are quite exciting as both newly synthesized dyes maintained their photovoltaic performance over an extended period compared to the commercial **MK 2** dye. Initially, the **YK 9** dye showed an inferior performance to **MK 2**, but with time, after 3000 h, **YK 9** outperformed **MK 2** in its PV performance. The higher open-circuit potential and short circuit current density endowed the **YK 8** sensitizer a higher PV performance than **YK 9** under 1 sun (100 mW cm^{-2}) conditions. The presence of more alkyl chains in the π-spacer and by virtue of its inherent molecular geometry, **YK 8** was efficient in controlling its aggregation, contributing to its better

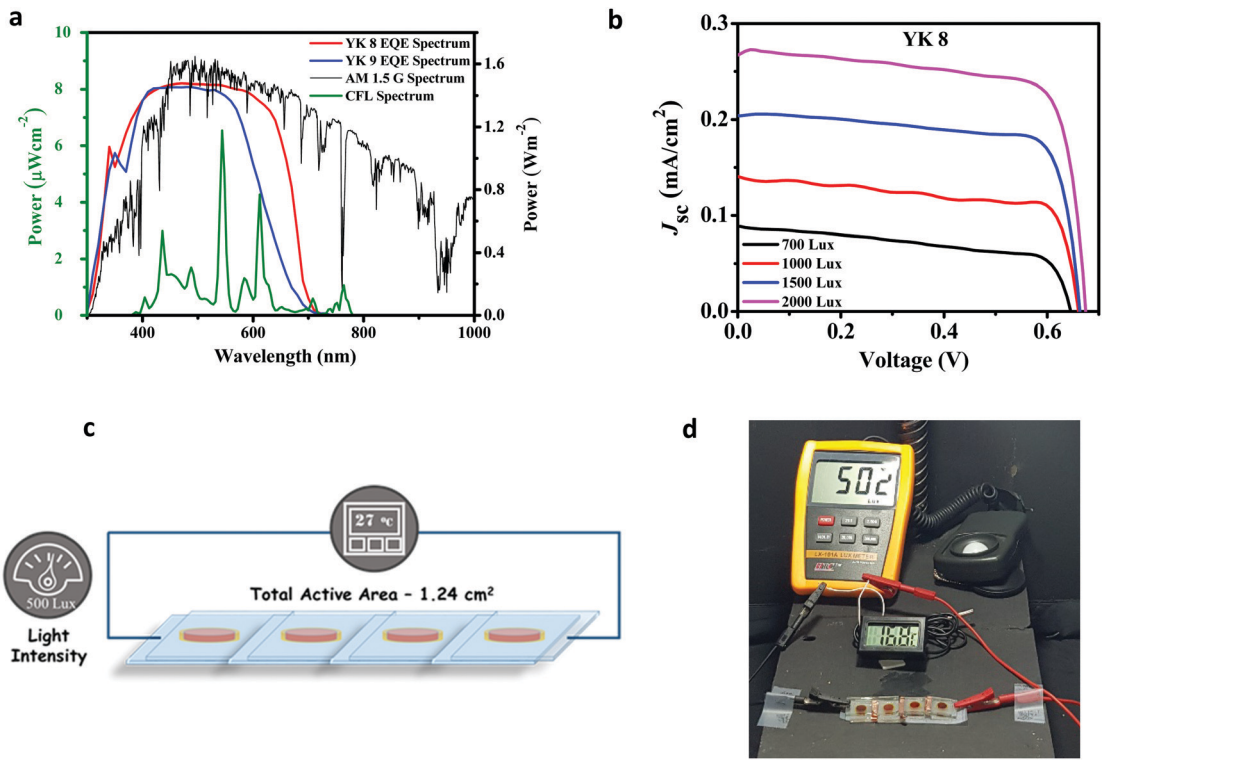

Fig. 6 (a) Power spectra of Osram 14 W T2 cool daylight fluorescent illumination overlapped with the EQE spectra of the **YK 8** and **YK 9** dyes and AM1.5G spectra. (b) Photovoltaic characteristics of DSCs under indoor-light source (Osram 14 W T2 cool daylight fluorescent tube illumination) for the **YK 8** sensitizer at 700 lux, 1000 lux, 1500 lux and 2000 lux. (c) Illustrative design and (d) image of self-powered temperature sensor coupled with four serially connected DSCs fabricated with the **YK 8** sensitizer at 500 lux (Osram 14 W T2 cool daylight fluorescent tube illumination).

lifetime and open circuit potential compared to that of **YK 9**. We carried out a range of electrical perturbation measurements to probe the charge transfer dynamics at various interfaces in the fabricated devices employing both the **YK 8** and **YK 9** dyes. This helped to gain a deeper understanding of the variations in current and voltage exhibited by both sensitizers and is discussed in detail in Section 2.6.

2.5. Indoor-light measurements

Unlike outdoor light conditions, indoor illumination is diverse in terms of magnitude and the spectrum of sources. Usually, the indoor/ambient illumination ranges between zero and 2000 lux, which is nearly equal to 0.02 sun. We carried out the indoor *J–V* measurements using Osram 14 W T2 cool daylight fluorescent tube illumination for the **YK 8** and **YK 9** dyes. The *J–V* plots under indoor fluorescent light illumination at various intensities (700 lux, 1000 lux, 1500 lux and 2000 lux) are displayed in Fig. 6b and Fig. S8a (ESI†) and the obtained PV parameters are summarized in Table 3. Below 700 lux, we observed larger fluctuations in output power using CFL lamps. The power spectrum of the indoor light source used in the present study overlapped with the EQE spectra of the **YK 8** and **YK 9** dyes and the AM1.5G spectra are shown in Fig. 6a. Under 1000 lux standard CFL illumination, **YK 8** realized a PCE of 28.7% ± 1.14% (P_{max} = 68.88 μW cm^{-2}, V_{oc} = 669 ± 7 mV, J_{sc} = 141 ± 3 μA cm^{-2}, and FF = 72.10% ± 1.28%) and **YK 9** attained a lower PCE of 14.21% ± 0.56% (P_{max} = 34.10 μW cm^{-2}, V_{oc} = 589 ± 7 mV, J_{sc} = 103 ± 2 μA cm^{-2}, and FF = 58.39% ± 1.55%) using the conventional iodide/triiodide electrolyte devoid of any co-sensitizers, which is better than the literature reports on related systems under similar testing conditions and device architecture (Table S6, ESI†). With a higher incident light intensity of 1500 lux, the **YK 8** sensitizer exhibited the maximum power conversion efficiency of 30.24% ± 1.23% (P_{max} = 108.85 μW cm^{-2}, V_{oc} = 679 ± 1 mV, J_{sc} = 200 ± 2 μA cm^{-2}, and FF = 80.03% ± 2.30%). The DSCs employing **YK 9** showed a maximum power conversion efficiency of 20.11% ± 0.96% (P_{max} = 96.53 μW cm^{-2}, V_{oc} = 619 ± 1 mV, J_{sc} = 208 ± 13 μA cm^{-2}, and FF = 76.08% ± 2.53%) at 2000 lux.

With an increase in light intensity (700 lux to 2000 lux), both the J_{sc} and V_{oc} increased for the **YK 8** and **YK 9** sensitizers. **YK 8** outperformed **YK 9** under indoor light conditions, which is mainly attributed to the higher voltage and current generated for the **YK 8** sensitizer under these conditions. More importantly, the red-shifted absorption in the range of 550–700 nm for the **YK 8** sensitizer, as evident from the EQE spectra, matches with the spectra of the cool daylight fluorescent tube illumination used in the present study (Fig. 6a), leading to better light harvesting. The use of thinner electrodes also reduces deep surface and trap states, contributing to a better PCE.[63,64] Additionally, the recombination process from existing sub-bandgap states also gets saturated at lower intensities, which can contribute to an improved lifetime and better charge collection efficiency, translating to a better current and voltage for the **YK 8** devices under indoor light. Thus, we have shown that in addition to the nature of the donor unit, the π-spacers also contribute to determining the performance of the organic dyes under indoor illumination. By preventing recombination, we can realize a higher shunt resistance, which improves the PV performance under low light illuminations. In the present contribution, **YK 8** offers more shunt resistance at 1500 lux, which may have also contributed to its better PCE at this particular light intensity. The shunt resistance follows the order of 700 lux (192.7 kΩ) < 1000 lux (254.6 kΩ) < 2000 lux (352.1 kΩ) < 1500 lux (520.8 kΩ). Under low illumination intensities, suitable control of recombination either by changing the dye or modifying the electrodes/electrolytes can lead to improved power conversion efficiencies. For comparison, the standard metal-free **MK 2** organic dye was also tested under similar conditions, which displayed an efficiency of 24.05% ± 0.47% at 1000 lux with J_{sc} = 132 ± 4 μA cm^{-2}, V_{oc} = 649 ± 7 mV and FF = 66.26% ± 1.20%, leading to a net power output of 57.72 μW cm^{-2}, and a PCE of 25.74 ± 0.46% was obtained at 1500 lux with J_{sc} = 195 ± 11 μA cm^{-2}, V_{oc} = 669 ± 6 mV and FF = 71.99 ± 1.69%, leading to a net power output of 92.65 μW cm^{-2} (Fig. S8b and c and Table S5, ESI†). Thus, **YK 8** displayed a better device performance than both the **YK 9** and commercial **MK 2** sensitizers under Osram 14 W T2 cool daylight fluorescent tube illumination. Under 1500 lux, **YK 8** yielded a 69.51% increase in PV performance compared to **YK 9** and 17.48% increment in the case of the **MK 2** dye.

To the best of our knowledge, the obtained efficiency for the **YK 8** sensitizer is among the best reported performances to date

Table 3 Tabulated photovoltaic data of DSCs with the **YK 8** and **YK 9** dyes under Osram 14 W T2 cool daylight fluorescent tube illumination at 700 lux, 1000 lux, 1500 lux and 2000 lux

Intensity (lux)	Input power (μW cm^{-2})	Output power (μW cm^{-2})	V_{oc} (mV)	J_{sc} (μA cm^{-2})	FF (%)	Efficiency (%)
YK 8						
700	160	35.43	649 ± 1	90 ± 2	60.70 ± 0.94	22.15 ± 0.42
1000	240	68.88	669 ± 7	141 ± 3	72.10 ± 1.28	28.70 ± 1.14
1500	360	108.85	679 ± 1	200 ± 2	80.03 ± 2.30	30.24 ± 1.23
2000	480	141.27	689 ± 1	270 ± 5	76.95 ± 1.46	29.43 ± 0.46
YK 9						
700	160	19.98	568 ± 7	69 ± 1	52.81 ± 1.37	12.49 ± 0.87
1000	240	34.10	589 ± 7	103 ± 2	58.39 ± 1.55	14.21 ± 0.56
1500	360	64.23	608 ± 6	154 ± 4	69.51 ± 2.26	17.84 ± 1.17
2000	480	96.53	619 ± 1	208 ± 13	76.08 ± 2.53	20.11 ± 0.96

for a DSC device using a single organic metal-free dye without co-sensitization, in combination with iodide/triiodide electrolyte under fluorescent tube illumination (<2000 lux) (Table S6, ESI†). A detailed comparison of the indoor photovoltaic performance of the **YK 8** and **YK 9** sensitizers with other dyes reported thus far, which were measured under similar indoor illumination conditions using iodide/triiodide electrolyte, is provided in Table S6 (ESI†) and a list of the highest reported indoor performances using DSCs is provided in Table S7 (ESI†). In addition to the higher indoor performance delivered by the **YK 8** sensitizer compared to the standard MK2 dye, the former was cheaper to synthesize. A detailed step-by-step cost calculation for the synthesis of the **YK 8** dye is provided in the ESI† (Table S8), which shows that one gram of **YK 8** can be synthesized at a lower price ($585 per gram) than many of the commercially available efficient organic sensitizers.

To demonstrate the real potential of these indoor/artificial light harvesters, we custom designed a fully functional self-powered temperature sensor with an LCD that draws power from the indoor solar cells made using the **YK 8** sensitizer. Four of these solar cells, each having an active area of 0.31 cm^2 were serially interconnected (net active area of 1.24 cm^2) to power the temperature sensor (Fig. S9, ESI†). An illumination of 500 lux provided by the fluorescent light source was enough to generate sufficient power to get the temperature sensor completely autonomous without any battery. An illustrative design of the developed setup is given in Fig. 6c and d, and a video is also provided.

2.6. Charge transfer dynamics

The open circuit voltage (V_{oc}) is an intrinsic property of a device, which is influenced by its structure, energetics and materials used for its fabrication. In DSCs, the energy difference between the Fermi level of TiO_2 and the redox potential of the electrolyte determines the V_{oc}.[65,66] In the present work, we employed iodide/triiodide redox electrolyte (redox potential 0.40 V *vs.* NHE) with both the **YK 8** and **YK 9** sensitizers. It is well-known that the electron concentration in a semiconductor determines its Fermi level.[67–69] With ample electrons, the Fermi level can lie very close to the conduction band (CB) of TiO_2. Again, the position of the TiO_2 CB and recombination are two key parameters that maintain TiO_2 Fermi level. Any minor change in electrolyte composition, sensitizer design and even TiO_2 preparation method influences the TiO_2 CB and rate of recombination.[70–72]

The TiO_2/dye/electrolyte interface is the most relevant interface in DSCs given that the injected electrons are prone to recombine with the holes present in the electrolyte and oxidised dye. It is imperative to investigate the TiO_2/dye/electrolyte interface to understand the origin of the variation in the open circuit potential. We probed the TiO_2/dye/electrolyte interface using electrochemical impedance spectroscopy (EIS) in

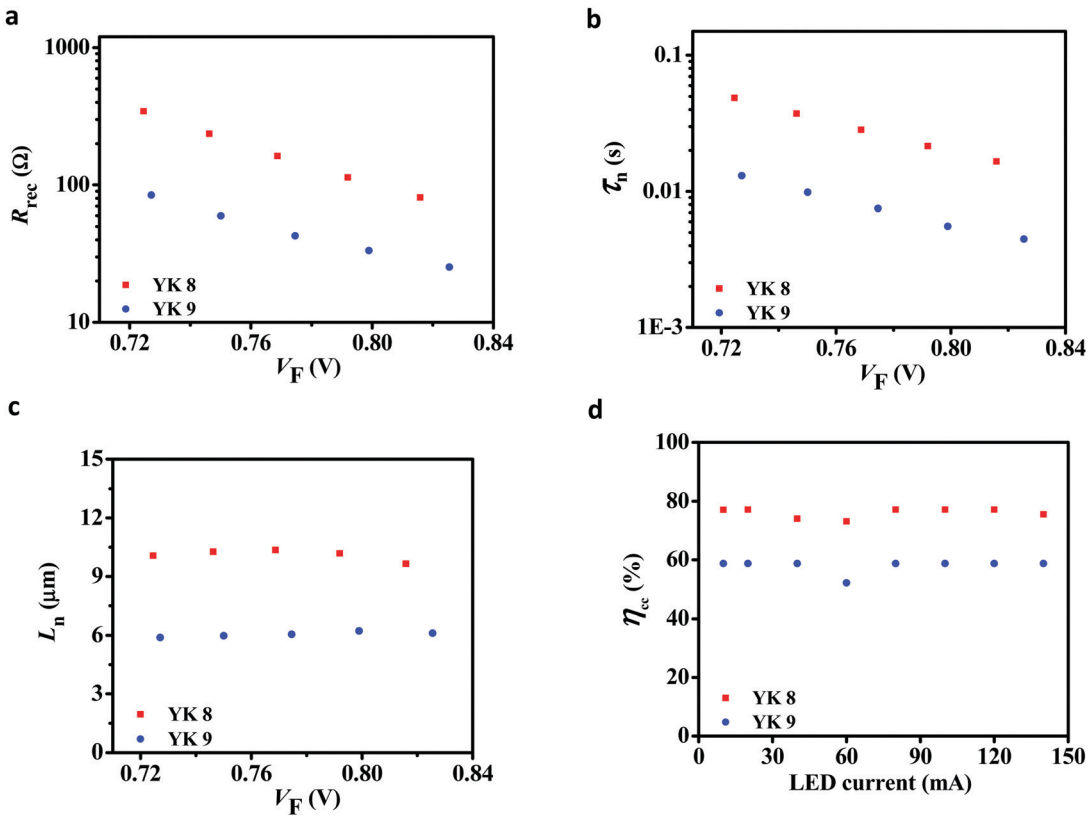

Fig. 7 (a) Recombination resistance (R_{rec}), (b) lifetime (τ_n) and (c) diffusion length (L_n) as function of corrected voltage (V_F) and (d) charge collection efficiency (η_{cc}) as a function of LED current for the **YK 8** and **YK 9** sensitizers.

the dark with a frequency ranging from 100 mHz to 100 kHz. The corresponding Nyquist plots are given in Fig. S10 (ESI†). The Nyquist plots were fitted using the transmission line model and analysed using the theory proposed by Bisquert *et al.*[73,74] Fig. S11 (ESI†) shows the relationship between the chemical capacitance (C_μ) and corrected voltage drop due to the series resistance (V_F). The chemical capacitance (C_μ) is commonly used to locate the position of the CB in TiO_2.[75–77] Both the **YK 8** and **YK 9** sensitizers showed almost similar capacitance values over the lower voltage range, which indicates that the conduction band of TiO_2 remained the same for both dyes and the variation in voltage is independent of the conduction band edge. The capacitance data for **YK 9** falls off at higher voltages. This can be due to some type of leakage of electrons for **YK 9** as a result of more recombination in **YK 9** compared to **YK 8**.

To probe the origin of the improvement in voltage for the **YK 8** sensitizer, we investigated the recombination resistance (R_{ct}) and lifetime (τ_n) in detail by EIS and IMVS measurements. **YK 8** showed a higher recombination resistance compared to **YK 9** (Fig. 7a). The lifetime results (Fig. 7b) exhibited the same trend following the recombination resistance. The **YK 8** dye having two dodecyl chains attached on the terthiophene π-spacer efficiently prevents the approach of oxidised species present in the electrolyte from coming close to the semiconductor in comparison to the **YK 9** dye, having a more planar thienothiophene spacer with only one dodecyl substituent. Thus, **YK 8** with more alkyl chains and a non-planar geometry forms a stronger shield against recombination, yielding a better electron lifetime. In addition, the better planarity of the **YK 9** dye will impart strong π–π interactions, resulting in more aggregation, as evident from the PV data obtained with variable CDCA concentrations (Fig. S4, ESI†), which leads to more recombination. The dark current measurement data given in Fig. S12 (ESI†) also supports this argument and is consistent with the lifetime plots, where the **YK 8** sensitizer showed a lower dark current compared to the **YK 9** dye. The lifetime was also measured using intensity modulated photovoltage spectroscopy (IMVS). Fig. S13 (ESI†) shows the lifetime from the IMVS measurements for the metal-free sensitizers, which followed the same trend as the EIS data. Fig. 7c shows the diffusion length (L_n) as a function of corrected voltage (V_F). The **YK 8** devices exhibited a better L_n compared to the **YK 9** devices. The electron diffusion length is defined as the average distance an electron is transported before it gets recombined. Thus, the better diffusion length translated into an improved charge collection efficiency (η_{cc}) for the **YK 8** sensitizer compared to **YK 9** (Fig. 7d).

Photo-induced absorption spectroscopy (PIA) is used to qualitatively study the electron injection from the oxidised dye to the CB of TiO_2 and regeneration of the oxidised dye by the reduced species present in the electrolyte. To evaluate the injection, the PIA spectra of the **YK 8**- and **YK 9**-soaked TiO_2 electrodes were analysed. Fig. 8a shows the PIA spectra of the dye-sensitized TiO_2. Both **YK 8** and **YK 9** show ground state bleach superimposed with a Stark shift at 530 nm. The interaction of the oxidised dye and injected electrons in TiO_2 induces a local electric field across the dye molecule, contributing to the Stark shift.[78–82] The absorption peak due to the oxidised dye molecule was observed at 780 nm for **YK 8** and 700 nm for **YK 9**. The absorption peak is observed when the excited electrons in the LUMO of the dye are injected to the CB of TiO_2. The visible absorption peak of the oxidised dye molecules for both sensitizers in the range of 650 nm to 850 nm indicates the efficient injection of electrons for both **YK 8** and **YK 9** sensitizers.

We carried out PIA measurements in electrolyte-filled devices for the regeneration study and compared them with the dye-soaked electrodes. Fig. 8b shows the PIA spectra of the dye alone and electrolyte-filled devices for **YK 8** and **YK 9**. In the electrolyte filled devices, the ground state bleach superimposed with a Stark shift was observed at 530 nm and 560 nm for **YK 8** and **YK 9**, respectively. As observed in Fig. 8b, the peak due to the absorption of the oxidised dye disappeared for both **YK 8** and **YK 9** with the addition of the electrolyte to the corresponding devices, which reveals that the oxidised ground state of the dye is efficiently regenerated by the reduced species present in the electrolyte for both the **YK 8** and **YK 9** sensitizers. The difference in intensities in PIA between the **YK 8** and **YK 9** dyes indicates that **YK 8** has a relatively higher injection and

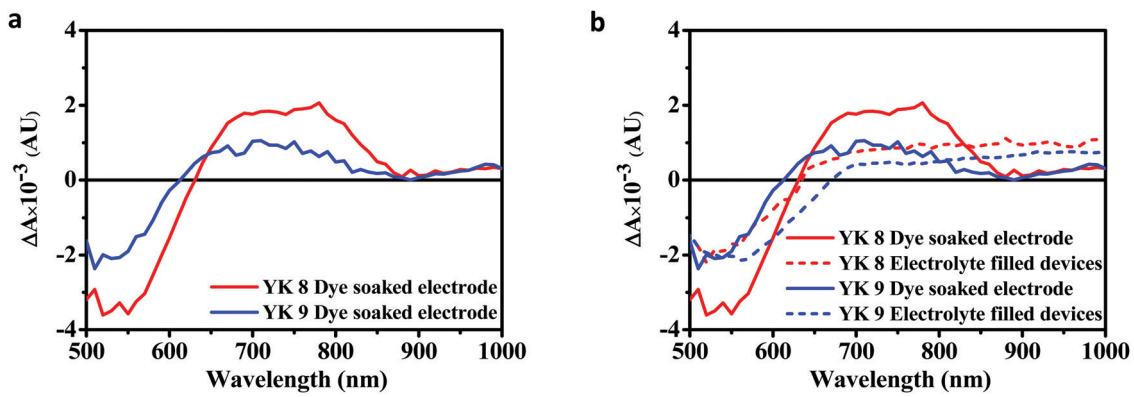

Fig. 8 PIA spectra of the **YK 8** and **YK 9** dyes (a) adsorbed on 6 μm TiO_2 film and (b) dye soaked 6 μm TiO_2 film electrodes and iodide/triiodide electrolyte-filled devices.

regeneration yield than **YK 9**, which also contributed to the better photovoltaic performance of **YK 8**.

Briefly, its low aggregation on the surface of TiO_2 and the added advantage of having more alkyl chains to prevent recombination assisted the **YK 8** dye to achieve an improved lifetime, leading to a better open-circuit voltage. In addition, the better diffusion length contributed to the superior charge collection efficiency of the **YK 8** sensitizer. Besides, the added advantage of a red-shifted absorption and relatively higher injection and regeneration yield helped **YK 8** in realizing a higher photovoltage and photocurrent in both full sun and indoor light conditions. Further, in addition to the higher performance under indoor illumination, the potential for scaling up the synthesis of the **YK 8** sensitizer at a lower cost compared to commercial standards renders immense possibilities to use this dye in modules/panels in the future.

3. Experimental

3.1. Materials and methods

The reagents and materials used for synthesis were of analytical grade and purchased from Ms Sigma-Aldrich, Ms Merck, and Ms Spectrochem Chemical, and used as received without further purification. All reactions were performed under an argon atmosphere. Before the Suzuki and Stille coupling reactions, any dissolved gas bubbles in the reaction mixture were removed by the freeze pump thaw method using liquid nitrogen and vacuum. The progress of the reaction was first assessed using thin layer chromatography on precoated Merck TLC silica gel 60 F254 silica plates. Purification of the product was done using column chromatography with 100–200 mesh Merck silica gel. ^{1}H and ^{13}C NMR spectra were recorded with a Bruker 500 MHz spectrometer using tetramethylsilane as the internal standard. Chemical shifts (δ) are given in ppm, and deuterated solvents were used for the measurements. Mass spectra of all the intermediates and final products were recorded on a Thermo Scientific Exactive spectrometer in electrospray ionization mass spectrometric (ESI) mode. IR spectra (ATR-FTIR or FTIR-KBr) were recorded using a Spectrum Two FTIR spectrometer by PerkinElmer. The structural characterization of the **YK 8** and **YK 9** dyes (^{1}H NMR, ^{13}C NMR, HRMS and ATR-FTIR) is presented in Fig. S15(i–xxxiv) (ESI†). Electronic absorption spectra were recorded on a UV-2600 UV-Vis spectrophotometer (Ms Shimadzu) using a 1 cm path length quartz cuvette. Cyclic voltammetry experiments were performed on a BAS 50 W voltammetric analyzer using 0.1 M tetrabutylammonium hexafluorophosphate in dichloromethane as the supporting electrolyte, glassy carbon working electrode, Ag/AgCl reference electrode, and platinum wire counter electrode. Density functional theory (DFT) calculations were performed at the B3LYP/6-311G/(d,p) level using the Gaussian 16 program.

3.2. Synthesis

3.2.1. Synthesis of compound 1. A solution of 2,5-bis(tributylstannyl)thiophene (500 mg, 0.76 mmol) and 2-bromo-3-octylthiophene (436 mg, 1.58 mmol) in 20 mL dry toluene was subjected to the freeze pump thaw method to remove dissolved oxygen and moisture. Then, $Pd_2(dba)_3$ (20 mg, 0.02 mmol) and P(*o*-tolyl)$_3$ (30 mg, 0.1 mmol) were added under an argon atmosphere and stirred under reflux overnight. The reaction mixture was then cooled to room temperature, diluted with dichloromethane, and subsequently washed with water and brine, and then dried over anhydrous Na_2SO_4. The crude mixture was purified by column chromatography over silica gel (100–200 mesh) using hexane as the eluent to afford the corresponding product **1** as a yellow oil. Yield (303 mg, 85%). Mass (ESI MS): 472.2292, found: 473.2287 (MH^+); ^{1}H NMR ($CDCl_3$, 500 MHz) δ/ppm = 7.17 (d, J = 5 Hz, 2H), 7.05 (s, 2H), 6.93 (d, J = 5 Hz, 2H), 2.78 (t, J = 7.5 Hz, 4H), 1.67–1.61 (m, 4H), 1.37–1.26 (m, 20H), 0.87 (t, J = 7 Hz, 6H); ^{13}C NMR ($CDCl_3$, 126 MHz) δ/ppm = 139.72, 136.07, 130.42, 130.08, 126.06, 123.74, 31.91, 30.78, 29.60, 29.48, 29.31, 22.70, 14.14; IR (KBr) ν in cm^{-1} = 2954, 2922, 2852, 1462, 1417, 1375, 1340, 1290, 1070, 1001, 960, 873, 831, 721, 690, 665, 594.

3.2.2. Synthesis of compound 2. To a solution of compound **1** (1 g, 2.12 mmol) and *N*,*N*-dimethylformamide (1.8 mL, 23.24 mmol) in 1,2-dichloroethane (20 mL), $POCl_3$ (0.3 mL, 3.2 mmol) was slowly added at 0 °C and stirred for 1 h under an argon atmosphere. Then, the reaction mixture was heated to 60 °C and stirred overnight. After cooling to room temperature, it was neutralized with $NaHCO_3$ (aq.), extracted using dichloromethane and dried over anhydrous Na_2SO_4. The crude product was purified by column chromatography over silica gel (100–200 mesh) using hexane as the eluent to afford product **2** as an orange oil. Yield 800 mg (76%). Mass (ESI MS): 500.2241, found: 501.2249 (MH^+); ^{1}H NMR ($CDCl_3$, 500 MHz) δ/ppm = 9.83 (s, 1H), 7.60 (s, 1H), 7.25 (d, J = 5 Hz, 1H), 7.22 (d, J = 5 Hz, 1H), 7.10 (d, J = 5 Hz, 1H), 6.95 (d, J = 5 Hz, 1H), 2.84–2.77 (m, 4H), 1.72–1.62 (m, 4H), 1.42–1.35 (m, 4H), 1.32–1.26 (m, 16H), 0.89–0.86 (m, 6H); ^{13}C NMR ($CDCl_3$, 126 MHz) δ/ppm = 182.59, 141.18, 140.40, 140.31, 140.19, 139.10, 138.51, 134.47, 130.26, 129.77, 127.80, 126.34, 124.41, 31.90, 31.87, 30.72, 30.35, 29.59, 29.51, 29.46, 29.42, 29.38, 29.29, 29.26, 22.69, 14.12; IR (KBr) ν in cm^{-1} = 2954, 2924, 2850, 1670, 1456, 1433, 1393, 1242, 1155, 858, 829, 798, 721, 675.

3.2.3. Synthesis of compound 3. To a stirred solution of compound **2** (500 mg, 1 mmol) in *N*,*N*-dimethylformamide (10 mL), and *N*-bromosuccinimide (266 mg, 1.5 mmol) were added in the dark and stirred at room temperature for 24 h. After completion of the reaction, the organic layer was extracted with dichloromethane, washed with $NaHCO_3$ (aq.), water and brine, and dried over anhydrous Na_2SO_4. The crude product was purified by column chromatography over silica gel (100–200 mesh) using hexane and dichloromethane (1 : 1, v/v) as the eluent to afford the corresponding product **3** as a yellow oil. Yield 400 mg (69%). Mass (ESI MS): 578.1346, found: 579.1421 (MH^+), 581.1398 ((M + 2) H^+); ^{1}H NMR ($CDCl_3$, 500 MHz) δ/ppm = 9.80 (s, 1H), 7.57 (s, 1H), 7.20 (d, J = 5 Hz, 1H), 7.00 (d, J = 5 Hz, 1H), 6.89 (s, 1H), 2.80–2.67 (m, 4H), 1.70–1.57 (m, 4H), 1.39–1.34 (m, 4H), 1.31–1.25 (m, 16H), 0.87–0.85 (m, 6H); ^{13}C NMR ($CDCl_3$, 126 MHz) δ/ppm = 182.59, 144.58,

141.46, 141.22, 138.88, 138.69, 136.31, 132.85, 131.76, 130.21, 127.35, 113.79, 112.95, 31.87, 30.4, 30.34, 29.50, 29.46, 29.42, 29.36, 29.32, 29.29, 29.25, 29.22, 29.20, 29.17, 26.93, 22.67, 14.12; IR (KBr) ν in cm^{-1} = 3079, 2960, 2920, 2850, 1662, 1491, 1467, 1409, 1390, 1332, 1261, 1245, 1156, 1097, 1023, 866, 844, 803, 690.

3.2.4. Synthesis of compound 4. To a solution of compound **3** (543 mg, 0.94 mmol), K_2CO_3 (276 mg in 1 mL water, 2 M), 9-methyl-9*H*-carbazole-3-boronic acid pinacol ester (288 mg, 0.94 mmol) was added. 20 mL of toluene was added to it and the entire system was subjected to freeze pump thawing to remove the dissolved oxygen. Then, $Pd(PPh_3)_4$ (30 mg, 0.03 mmol) was added under an argon atmosphere and refluxed for 18 h. The reaction mixture was extracted with dichloromethane and purified by column chromatography over silica gel (100–200 mesh) using dichloromethane and hexane (1 : 4, v/v) as the eluent to yield compound **4** as a red solid. Yield 565 mg (88%). Mass (ESI MS): 679.2976, found: 679.2970 (MH^+); ^{1}H NMR (500 MHz, $CDCl_3$) δ/ppm = 9.83 (s, 1H), 8.32 (s, 1H), 8.14 (d, J = 8 Hz, 1H), 7.74 (dd, J = 2, 8 Hz, 1H), 7.61 (s, 1H), 7.51 (m, 1H), 7.42 (t, J = 7 Hz, 2H), 7.27 (m, 2H), 7.23 (s, 1H), 7.16 (d, J = 4 Hz, 1H), 3.88 (s, 3H), 2.87–2.82 (m, 4H), 1.78–1.68 (m, 4H), 1.48–1.41 (m, 4H), 1.38–1.26 (m, 16H), 0.89–0.87 (m, 6H); ^{13}C NMR ($CDCl_3$, 126 MHz) δ/ppm = 182.48, 144.25, 143.19, 141.53, 141.41, 141.36, 140.75, 140.21, 140.12, 139.06, 138.96, 128.05, 127.89, 126.92, 125.73, 125.22, 123.97, 123.30, 122.73, 120.50, 119.27, 117.53, 108.81, 108.71, 31.94, 31.89, 30.68, 30.36, 29.84, 29.72, 29.54, 29.52, 29.44, 29.33, 29.28, 29.26, 22.71, 22.68, 14.12; IR (KBr) ν in cm^{-1} = 3057, 2954, 2924, 2848, 1664, 1539, 1483, 1427, 1393, 1334, 1249, 1153, 1062, 871, 806, 781, 742, 723, 667.

3.2.5. Synthesis of YK 8. Compound **4** (200 mg, 0.3 mmol) and cyanoacetic acid (130 mg, 1.5 mmol) were dissolved in 20 mL dry chloroform. Then two drops of piperidine were added to this mixture and stirred at 45 °C for 40 h. The reaction mixture was extracted with chloroform, washed with water, dried over anhydrous Na_2SO_4 and purified by column chromatography over silica gel (100–200 mesh) using chloroform and methanol (9 : 1, v/v) as the eluent to give compound **YK 8**. Yield 171 mg (78%). Mass (ESI MS): 746.3034, found: 747.3112 (MH^+); ^{1}H NMR (500 MHz, DMSO-d_6) δ/ppm = 8.42 (s, 1H), 8.30 (s, 1H), 8.20 (d, J = 8 Hz, 1H), 7.78 (s, 1H), 7.71 (d, J = 8.5 Hz, 1H), 7.57 (t, J = 8 Hz, 2H), 7.48 (t, J = 7.5 Hz, 1H), 7.42 (s, 1H), 7.34 (s, 1H), 7.24–7.21 (m, 2H), 3.85 (s, 3H), 2.81 (t, J = 7 Hz, 4H), 1.72–1.63 (m, 4H), 1.40–1.24 (m, 20H), 0.83 (m, 6H); ^{13}C NMR (DMSO-d6, 126 MHz) δ/ppm = 164.04, 144.04, 143.06, 141.65, 140.43, 138.49, 134.40, 133.08, 129.29, 127.44, 126.77, 126.22, 124.47, 123.93, 122.99, 121.03, 119.75, 110.21, 109.87, 99.00, 31.73, 31.71, 30.31, 29.97, 29.56, 29.39, 29.18, 29.13, 29.07, 28.97, 22.53, 14.36; ATR-FTIR ν in cm^{-1} = 2920, 2850, 2216, 1680, 1563, 1397, 1267, 1248, 1211, 1169, 1152, 931, 870, 789, 742, 723, 650.

3.2.6. Synthesis of compound 5. To a stirred solution of thieno[3,2-*b*]thiophene (500 mg, 3.6 mmol) in 20 mL dry THF, 2.0 M *n*-BuLi in hexane (1.78 mL, 3.6 mmol) was added at −78 °C under an Ar atmosphere. After 1.5 h, 2-isopropoxy-4,4,5,5-tetramethyl-4,3,2-dioxaboralane (0.8 mL, 3.9 mmol) was added and the reaction was allowed to warm to room temperature. After 12 h of stirring, the reaction was quenched with saturated NH_4Cl solution. The reaction mixture was extracted using dichloromethane and water, dried over anhydrous Na_2SO_4 and purified by column chromatography over silica gel (100–200 mesh) using a mixture of ethyl acetate and hexane (1 : 20, v/v) as the eluent to afford product **5** as a yellow solid. Yield 300 mg (30%). Mass (ESI MS): 266.0606, found: 267.0687 (MH^+); ^{1}H NMR ($CDCl_3$, 500 MHz) δ/ppm = 7.76 (s, 1H), 7.48 (d, J = 5.5 Hz, 1H), 7.28 (d, J = 5.5 Hz, 1H), 1.36 (s, 12H); ^{13}C NMR ($CDCl_3$, 126 MHz) δ/ppm = 145.58, 140.83, 130.02, 128.98, 119.49, 84.30, 30.94, 24.77; IR (KBr) ν in cm^{-1} = 3103, 3084, 2976, 2933, 1506, 1460, 1357, 1265, 1139, 1018, 958, 906, 850, 827, 771, 665.

3.2.7. Synthesis of compound 6. To a solution of compound 2-bromo-3-octylthiophene (500 mg, 1.8 mmol) and *N*,*N*-dimethylformamide (1.4 mL, 18 mmol) in 1,2-dichloroethane (20 mL), $POCl_3$ (0.3 mL, 3.2 mmol) was slowly added at 0 °C and stirred for 1 h under an argon atmosphere. Then, the reaction mixture was heated to 60 °C and stirred overnight. After cooling to room temperature, it was neutralized with $NaHCO_3$ (aq.), extracted using chloroform and dried over anhydrous Na_2SO_4. The crude product was purified by column chromatography over silica gel (100–200 mesh) using chloroform:hexane (1 : 20) as the eluent to afford product **6** as an orange oil. Yield 500 mg (90%). Mass (ESI MS): 302.0339, found: 303.0428 (MH^+), 305.0407 ((M + 2) H^+); ^{1}H NMR (500 MHZ, $CDCl_3$) δ/ppm = 9.75 (s, 1H), 7.46 (s, 1H), 2.59 (t, J = 7.75 Hz, 2H), 1.62–1.59 (m, 2H), 1.32–1.23 (m, 10H), 0.88 (t, J = 6.5 Hz, 3H); ^{13}C NMR (DMSO-d_6, 126 MHz) δ/ppm = 177.16, 139.24, 138.13, 132.06, 117.38, 27.10, 24.73, 24.72,24.57,24.45, 24.39, 17.91, 9.36; IR (KBr) ν in cm^{-1} = 3089, 2956, 2922, 2870, 1665, 1600, 1531, 1456, 1384, 1253, 1120, 1043, 867, 798, 675.

3.2.8. Synthesis of compound 7. A solution containing compound **5** (600 mg, 2.3 mmol), compound **6** (700 mg, 2.3 mmol) and K_2CO_3 (934 mg, 6.8 mmol) in toluene (20 mL) was subjected to the freeze pump thaw method to remove oxygen and moisture. Then, a palladium catalyst [$Pd(PPh_3)_4$] (30 mg, 0.03 mmol) was added to it and stirred at 110 °C for 48 h. The mixture was poured into water and extracted using $CHCl_3$. The combined organic layer was washed with water, dried with anhydrous sodium sulphate and purified by column chromatography over silica gel (100–200 mesh) using chloroform and hexane (2 : 3) to give compound **7** as a yellow solid. Yield 483 mg (58%). Mass (ESI MS): 362.0832, found: 363.0914 (MH^+); ^{1}H NMR (500 MHz, $CDCl_3$) δ/ppm = 9.84 (s, 1H), 7.61 (s, 1H), 7.44 (d, J = 8 Hz, 2H), 7.27 (d, J = 6 Hz, 1H), 2.83 (t, J = 7.75 Hz, 2H), 1.70–1.67 (m, 2H), 1.41–1.26 (m, 10H), 0.88 (t, J = 7 Hz, 3H); ^{13}C NMR ($CDCl_3$, 126 MHz) δ/ppm = 182.64, 141.39, 140.87, 140.82, 140.40, 139.62, 138.93, 128.53, 119.64, 119.41, 31.85, 30.43, 29.46, 29.38, 29.32, 29.22, 22.67, 14.12; IR (KBr) ν in cm^{-1} = 3130, 3082, 2943, 2926, 2848, 1651, 1525, 1496, 1465, 1417, 1386, 1336, 1246, 1165, 956, 871, 812, 742, 707, 682, 640.

3.2.9. Synthesis of compound 8. To a stirred solution of 1.3 g of 7 (3.58 mmol) in acetic acid and dry chloroform (1 : 1, v/v), NBS (637 mg, 3.58 mmol) was added and stirred for

2 h in the dark at 25 °C. The reaction was quenched using water and sodium bicarbonate solution, extracted with chloroform, washed with water, dried over anhydrous sodium sulphate and purified by column chromatography over silica gel (100–200 mesh) using chloroform and hexane (2 : 3) as the eluent to give compound **8** as a yellow solid. Yield 1.09 g (69%). Mass (ESI MS): 439.9937, found: 441.0019 (MH^+), 442.9996 ((M + 2) H^+); ^{1}H NMR (500 MHZ, $CDCl_3$) δ/ppm = 9.84 (s, 1H), 7.61 (s, 1H), 7.33 (s, 1H), 7.27 (s, 1H), 2.80 (t, J = 7.75 Hz, 2H), 1.69–1.61 (m, 2H), 1.39–1.25 (m, 10H), 0.88 (t, J = 7 Hz, 3H); ^{13}C NMR ($CDCl_3$, 126 MHz) δ/ppm = 182.62, 141.05, 140.97, 140.71, 139.76, 139.13, 138.92, 135.95, 122.08, 119.10, 115.03, 31.85, 30.39, 29.44, 29.37, 29.33, 29.22, 22.67, 14.13; IR (KBr) ν in cm^{-1} = 3097, 2956, 2922, 2852, 1662, 1541, 1490, 1467, 1409, 1390, 1330, 1246, 1159, 987, 869, 802, 744, 677.

3.2.10. Synthesis of compound 9. To a solution of compound **8** (500 mg, 1.13 mmol), K_2CO_3 (276 mg in 1 mL water, 2 M), 9-methyl-9*H*-carbazole-3-boronic acid pinacol ester (347 mg, 1.13 mmol) was added. Then 20 mL of toluene was added to it and the entire system was subjected to the freeze pump thaw method to remove the dissolved oxygen. Then, $Pd(PPh_3)_4$ (30 mg, 0.03 mmol) was added under an argon atmosphere and refluxed for 18 h. The reaction mixture was extracted with chloroform and purified by column chromatography over silica gel (100–200 mesh) using dichloromethane and hexane (1 : 4, v/v) as eluent to yield compound **9** as a red solid. Yield 530 mg (84%). Mass (ESI MS): 541.1567, found: 542.1649 (MH^+); ^{1}H NMR (500 MHz, $CDCl_3$) δ/ppm = 9.84 (s, 1H), 8.35 (d, J = 1.5 Hz, 1H), 8.15 (d, J = 7.5 Hz, 1H), 7.78 (dd, J = 2 Hz, 1H) 7.62 (s, 1H), 7.54–7.51 (m, 2H), 7.45–7.42 (m, 3H), 7.29 (d, J = 7.5 Hz, 1H), 3.89 (s, 3H), 2.86 (t, J = 8 Hz, 2H), 1.75–1.68 (m, 2H), 1.43–1.25 (m, 10H), 0.89 (t, J = 6.75 Hz, 3H); ^{13}C NMR ($CDCl_3$, 126 MHz) δ/ppm = 182.58, 149.31, 141.80, 141.55, 141.52, 140.94, 140.52, 139.11, 138.03, 135.07, 126.30, 125.57, 124.20, 123.34, 122.62, 120.53, 119.84, 119.40, 117.92, 113.98, 108.97, 108.78, 31.88, 30.39, 29.71, 29.51, 29.41, 29.26, 26.93, 22.69, 14.14, 14.11; IR (KBr) ν in cm^{-1} = 3097, 3080, 2961, 2921, 2849, 1663, 1534, 1491, 1467, 1409, 1390, 1331, 1261, 1245, 1156, 897, 866, 842, 803, 745, 677.

3.2.11. Synthesis of YK 9. Compound **9** (300 mg, 0.55 mmol) and cyanoacetic acid (234 mg, 2.75 mmol) were dissolved in 20 mL dry chloroform. Then, two drops of piperidine were added to this and stirred at 45 °C for 40 h. The reaction mixture was extracted with chloroform, washed with water, dried over anhydrous Na_2SO_4 and purified by column chromatography using chloroform and methanol (9 : 1, v/v) as the eluent to give compound **YK 9**. Yield 287 mg (86%). Mass (ESI MS): 608.1625, found: 609.1684 (MH^+); ^{1}H NMR (500 MHz, DMSO-d_6) δ/ppm = 8.49 (s, 1H), 8.24 (d, 1H, 7.5 Hz), 8.15 (s, 1H), 7.86 (s, 1H), 7.79 (d, J = 8 Hz, 1H), 7.69 (d, J = 6.6 Hz, 2H), 7.63–7.59 (m, 2H) 7.52–7.49 (m, 1H), 7.26–7.23 (m, 1H), 3.87 (s, 3H), 2.78 (t, J = 7.5 Hz, 2H), 1.61 (t, J = 7 Hz 2H), 1.32–1.19 (m, 10H), 0.81 (t, J = 6.5 Hz, 3H); ^{13}C NMR (DMSO-d_6, 126 MHz) δ/ppm = 164.25, 148.84, 141.63, 141.18, 140.96, 140.37, 138.20, 134.88, 134.39, 127.49, 126.80, 125.32, 124.17, 123.01, 122.28, 121.10, 120.73, 119.70, 117.74, 117.12, 115.09, 110.34, 109.92, 31.72, 29.97, 29.57, 29.14, 29.07, 28.86, 22.54, 14.41; ATR-FTIR ν in cm^{-1} = 2923, 2852, 2212, 1680, 1574, 1478, 1385, 1366, 1300, 1249, 796, 766, 745, 726, 674.

3.3. Device fabrication and characterization

Fluorine-doped tin oxide (FTO, TEC 15 Ω Sq^{-1} cm^{-1}) glass (GreatCell Solar) were used as the substrate. The substrates were cleaned in detergent, deionized water, isopropyl alcohol, and acetone using an ultrasonic bath. Subsequently, the electrodes were annealed at 500 °C, followed by UV-ozone cleaning. The cleaned electrodes were immersed in 40 mM $TiCl_4$ at 70 °C for 30 min to coat an ultra-thin blocking layer over FTO. Then the substrates were rinsed in de-ionized water and ethanol, followed by annealing at 500 °C. A TiO_2 layer was coated using the doctor-blading technique. After the deposition of TiO_2, the substrates were heat-treated at a ramped heating rate (325 °C for 15 min, 375 °C for 15 min, 450 °C for 15 min and 500 °C for 30 min). Devices with two different TiO_2 (GreatCell Solar) layer architectures, *i.e.*, single layer (1L) and bilayer (1L + S), were fabricated. 1L contained a 6 μm TiO_2 (18 NR-T) transparent layer, and 1L + S contained 10 μm TiO_2 (6 μm 18 NR-T and 4 μm scattering 18 NR-AO) layer. The optimized semiconductor layer thickness was 1L (6 μm) for the best-performing devices. Further, a blocking layer over TiO_2 was deposited by adopting the same procedure used for deposition of the pre-blocking layer. The electrodes were immersed in the respective dye solutions (**YK 8**, **YK 9** and **MK 2**) with a dye concentration of 0.3 mM in toluene for 15 h. For the counter electrode (CE), platinum (Platisol, GreatCell Solar) was coated on pre-drilled fluorine-doped tin oxide (TEC 7 Ω Sq^{-1} cm^{-1}) glass using a painting brush, and then annealed at 400 °C for 30 min. The working electrode and counter electrode were assembled using 25 μm-thick Surlyn. The space between the electrodes was filled using the standard I^-/I_3^- electrolyte (HPE, GreatCell Solar). The holes at the counter electrode were sealed using a cover glass.

The thickness of the semiconductor layer (TiO_2) was measured using a Bruker-DektakXT surface profiler. The current density *versus* voltage (*J–V*) curve of the fabricated DSCs was measured under AM1.5G irradiation (100 mW cm^{-2}) using a Newport class AAA solar simulator (Fig. S16 (ESI†), Oriel Sol3A-94023A) calibrated with a standard silicon solar cell (Fig. S17, ESI†) at room temperature. To avoid the overestimation of J_{sc} due to stray light, during all the photovoltaic characterizations, we used a black mask with an aperture of 0.1256 cm^2 (radius of 2 mm) over the device with a total active area of 0.31 cm^2. Also, all the photovoltaic results reported are from the data obtained from 8 devices, and the error was estimated using the standard deviation method. For the stability measurements, the devices were kept at open circuit at room temperature (27 °C) under >70% humidity condition, and the measurements were done at equal intervals (500 h) using a class AAA Newport solar simulator. The incident photon-to-current conversion efficiency (IPCE) measurements were carried out in DC mode (Newport, 350 W Xenon lamp, Fig. S18 and S19, ESI†). The low-light (indoor-light)

measurements were performed in a home-made indoor light measurement setup (Fig. S14, ESI†) using an Osram 14 W T2 cool daylight fluorescent tube as the illumination source ranging between zero and 2000 lux. The light intensity was calibrated and measured using a high sensitivity certified irradiance measuring unit from Dyenamo AB (DN-AE06). The *J–V* measurements under lower intensities were performed using a certified low power measuring unit from Dyenamo AB, which was custom made for carrying out low-light (indoor ambient light) measurements with maximum accuracy (DN-AE05). Electrochemical impedance spectroscopy (EIS) measurements of the DSCs were carried out using an Autolab (PGSTAT 302N) workstation equipped with an FRA under forward bias in the dark. The impedance plots were recorded from 0.72 V to 0.80 V, with 200 mV increments and corrected for the voltage drop due to series resistance for representing the derived parameter from EIS. The perturbation bias was 10 mV AC potential in the frequency range of 0.1 Hz to 100 kHz in equally spaced logarithmic steps. The circuit fitting was carried out using the NOVA 1.11 software. Intensity-modulated photovoltage spectroscopy (IMVS) measurements were carried out using an electrochemical workstation (PGSTAT 302N) equipped with an FRA and LED driver. The photovoltage response of the devices was recorded in the frequency range of 1 Hz to 1 kHz. The amplitude of the sinusoidal modulation for IMVS measurement was 10% of the DC light. PIA was carried out using equipment custom developed by Dynamo AB (Sweden), which uses a 1 W blue light-emitting LED (λ = 470 nm) as the pump and 20 W tungsten halogen lamp as the probe. The transmitted light through the sample is focused on a monochromator and detected by a UV-enhanced Si detector connected to a lock-in amplifier (SR830) *via* a current amplifier. The PIA spectra of the devices were recorded using excitation by LED, which was a square wave with a modulation frequency of 9.3 Hz. For the PIA measurements, the TiO_2 thickness was kept at 6 μm.

4. Conclusions

In conclusion, the **YK 8** dye with bis-octyl terthiophene proved to be a good candidate in preventing recombination compared to the mono-octyl-substituted thiophene spacer in the **YK 9** dye. Both dyes were exceptionally stable and delivered their best performance after ageing for 4 months. Using 1000 lux standard CFL illumination, **YK 8** realized a PCE of 28.7% and **YK 9** exhibited a PCE of 14.21% using the conventional iodide/triiodide electrolyte devoid of any co-sensitizers. A maximum PCE of 30.24% was exhibited by the **YK 8** dye at a higher illumination intensity of 1500 lux with a power output of 108.85 μW cm^{-2} under Osram T2 cool daylight fluorescent tube illumination. **YK 9** displayed a PCE of 17.84% under 1500 lux fluorescent tube illumination. The better lifetime by virtue of the additional octyl chains present in the terthiophene π-spacer along with the added advantage of proper molecular orientation and precise control over aggregation effectively impeded recombination in the **YK 8** dye. This translated into higher open circuit potential and improved light-harvesting ability in the visible region for **YK 8**. The close match of the **YK 8** absorption with the fluorescent tube spectra also led to an improved J_{sc} compared to **YK 9**. Additionally, its better diffusion length, improved charge collection efficiency and relatively higher injection and regeneration yield helped **YK 8** dye to outperform **YK 9** and commercial **MK 2** metal-free sensitizer both under indoor light and full sun conditions. To demonstrate the potential of these artificial light harvesting solar cells, mini-modules were fabricated by serially interconnecting DSCs sensitized with the **YK 8** dye. The serially connected module with a total active area of 1.24 cm^2 generated sufficient power even at a very low light intensity of 500 lux fluorescent lamp illumination to realize a completely self-powered temperature sensor with an LCD display, unveiling the real potential of these custom-designed dyes for indoor photovoltaics. The scale-up capability of these organic dyes at a lower cost further suggests their potential widespread application in indoor light harvesting.

Author contributions

Dyes were designed and characterized by KY, RH and AV. Photovoltaic measurements were designed by SS. Solar cells fabricated, measured and analysed by VJ and SCP. SS, KNNU and AA supervised the project. SS wrote the manuscript with inputs from all authors.

Conflicts of interest

There are no conflicts of interest to declare.

Acknowledgements

S. S., N. U. K. N., Y. K. and A. A. thank DST for the support under DST-SERB Project [DST/SERB/F/481]. A. A. is grateful to the DST-SERB, Govt. of India, for a J. C. Bose National Fellowship [SB/S2/JCB-11/2014]. S. S. acknowledges financial support from DST-CRG (CRG/2020/001406) and CSIR-FIRST (MLP65) projects. J. V. and S. C. P. thank DST-SERB and DST-SERI for research fellowships. R. H. thanks CSIR for research fellowship. Prof. Anders Hagfeldt is acknowledged for the scientific discussions and feedbacks.

References

1 World Energy Issues Monitor 2020, 2020.
2 BP Statistical Review of World Energy, 2019.
3 L. Roselli, N. Borges Carvalho, F. Alimenti, P. Mezzanotte, G. Orecchini, M. Virili, C. Mariotti, R. Goncalves and P. Pinho, *Proc. IEEE*, 2014, **102**, 1723–1746.
4 E. Hittinger and P. Jaramillo, *Science*, 2019, **364**, 326–328.
5 H. Sun, M. Yin, W. Wei, J. Li, H. Wang and X. Jin, *Microsyst. Technol.*, 2018, **24**, 2853–2869.

6 M. Prauzek, J. Konecny, M. Borova, K. Janosova, J. Hlavica and P. Musilek, *Sensors*, 2018, **18**, 2446.
7 R. Haight, W. Haensch and D. Friedman, *Science*, 2016, **353**, 124–125.
8 A. Hagfeldt, G. Boschloo, L. Sun, L. Kloo and H. Pettersson, *Chem. Rev.*, 2010, **110**, 6595–6663.
9 B. P. Lechêne, M. Cowell, A. Pierre, J. W. Evans, P. K. Wright and A. C. Arias, *Nano Energy*, 2016, **26**, 631–640.
10 I. Mathews, S. N. Kantareddy, T. Buonassisi and I. M. Peters, *Joule*, 2019, **3**, 1415–1426.
11 R. Cheng, C. Chung, H. Zhang, F. Liu, W. Wang, Z. Zhou, S. Wang, A. B. Djurišić and S. Feng, *Adv. Energy Mater.*, 2019, **9**, 1901980.
12 G. Kim, J. W. Lim, J. Kim, S. J. Yun and M. A. Park, *ACS Appl. Mater. Interfaces*, 2020, **12**, 27122–27130.
13 X. He, J. Chen, X. Ren, L. Zhang, Y. Liu, J. Feng, J. Fang, K. Zhao and S. (Frank) Liu, *Adv. Mater.*, 2021, **33**, 2100770.
14 M. Li, F. Igbari, Z. Wang and L. Liao, *Adv. Energy Mater.*, 2020, **10**, 2000641.
15 A. Virtuani, E. Lotter, M. Powalla, U. Rau and J. H. Werner, *Thin Solid Films*, 2004, **451–452**, 160–165.
16 A. S. Teran, E. Moon, W. Lim, G. Kim, I. Lee, D. Blaauw and J. D. Phillips, *IEEE Trans. Electron Devices*, 2016, **63**, 2820–2825.
17 A. S. Teran, J. Wong, W. Lim, G. Kim, Y. Lee, D. Blaauw and J. D. Phillips, *IEEE Trans. Electron Devices*, 2015, **62**, 2170–2175.
18 Y. Cui, Y. Wang, J. Bergqvist, H. Yao, Y. Xu, B. Gao, C. Yang, S. Zhang, O. Inganäs, F. Gao and J. Hou, *Nat. Energy*, 2019, **4**, 768–775.
19 Z. Ding, R. Zhao, Y. Yu and J. Liu, *J. Mater. Chem. A*, 2019, **7**, 26533–26539.
20 G. D. Barber, P. G. Hoertz, S. H. A. Lee, N. M. Abrams, J. Mikulca, T. E. Mallouk, P. Liska, S. M. Zakeeruddin, M. Grätzel, A. Ho-Baillie and M. A. Green, *J. Phys. Chem. Lett.*, 2011, **2**, 581–585.
21 H. Michaels, M. Rinderle, R. Freitag, I. Benesperi, T. Edvinsson, R. Socher, A. Gagliardi and M. Freitag, *Chem. Sci.*, 2020, **11**, 2895–2906.
22 Y. Cao, Y. Liu, S. M. Zakeeruddin, A. Hagfeldt and M. Grätzel, *Joule*, 2018, **2**, 1108–1117.
23 A. Venkateswararao, J. K. W. Ho, S. K. So, S.-W. Liu and K.-T. Wong, *Mater. Sci. Eng., R*, 2020, **139**, 100517.
24 Y. S. Tingare, N. S. Vinh, H.-H. Chou, Y.-C. Liu, Y.-S. Long, T.-C. Wu, T.-C. Wei and C.-Y. Yeh, *Adv. Energy Mater.*, 2017, **7**, 1700032.
25 M. Freitag, J. Teuscher, Y. Saygili, X. Zhang, F. Giordano, P. Liska, J. Hua, S. M. Zakeeruddin, J.-E. E. Moser, M. Grätzel and A. Hagfeldt, *Nat. Photonics*, 2017, **11**, 372–378.
26 Y. Liu, Y. Cao, W. Zhang, M. Stojanovic, M. I. Dar, P. Péchy, Y. Saygili, A. Hagfeldt, S. M. Zakeeruddin and M. Grätzel, *Angew. Chem., Int. Ed.*, 2018, **57**, 14125–14128.
27 D. Zhang, M. Stojanovic, Y. Ren, Y. Cao, F. T. Eickemeyer, E. Socie, N. Vlachopoulos, J.-E. Moser, S. M. Zakeeruddin, A. Hagfeldt and M. Grätzel, *Nat. Commun.*, 2021, **12**, 1777.
28 T. W. Hamann, R. A. Jensen, A. B. F. Martinson, H. Van Ryswyk and J. T. Hupp, *Energy Environ. Sci.*, 2008, **1**, 66–78.
29 K. Zeng, Z. Tong, L. Ma, W. H. Zhu, W. Wu, Y. Xie and Y. Xie, *Energy Environ. Sci.*, 2020, **13**, 1617–1657.
30 J. H. Yum, E. Baranoff, S. Wenger, M. K. Nazeeruddin and M. Grätzel, *Energy Environ. Sci.*, 2011, **4**, 842–857.
31 M.-W. Lee, J.-Y. Kim, H. J. Son, J. Y. Kim, B. Kim, H. Kim, D.-K. Lee, K. Kim, D.-H. Lee and M. J. Ko, *Sci. Rep.*, 2015, **5**, 7711.
32 A. Yella, H.-W. Lee, H. N. Tsao, C. Yi, A. K. Chandiran, M. K. Nazeeruddin, E. W.-G. Diau, C.-Y. Yeh, S. M. Zakeeruddin and M. Gratzel, *Science*, 2011, **334**, 629–634.
33 S. Mathew, A. Yella, P. Gao, R. Humphry-Baker, B. F. E. Curchod, N. Ashari-Astani, I. Tavernelli, U. Rothlisberger, M. K. Nazeeruddin and M. Grätzel, *Nat. Chem.*, 2014, **6**, 242–247.
34 N. Robertson, *Angew. Chem., Int. Ed.*, 2006, **45**, 2338–2345.
35 K. Zeng, Y. Chen, W. H. Zhu, H. Tian and Y. Xie, *J. Am. Chem. Soc.*, 2020, **142**, 5154–5161.
36 Y. Kurumisawa, T. Higashino, S. Nimura, Y. Tsuji, H. Iiyama and H. Imahori, *J. Am. Chem. Soc.*, 2019, **141**, 9910–9919.
37 H. Song, Q. Liu and Y. Xie, *Chem. Commun.*, 2018, **54**, 1811–1824.
38 S. Ahmad, E. Guillén, L. Kavan, M. Grätzel and M. K. Nazeeruddin, *Energy Environ. Sci.*, 2013, **6**, 3439–3466.
39 Y. S. Yen, H. H. Chou, Y. C. Chen, C. Y. Hsu and J. T. Lin, *J. Mater. Chem.*, 2012, **22**, 8734–8747.
40 A. Carella, F. Borbone and R. Centore, *Front. Chem.*, 2018, **6**, 1–24.
41 A. Baumann, C. Curiac and J. H. Delcamp, *ChemSusChem*, 2020, **13**, 2503–2512.
42 K. Kakiage, Y. Aoyama, T. Yano, K. Oya, J. I. Fujisawa and M. Hanaya, *Chem. Commun.*, 2015, **51**, 15894–15897.
43 M. V. Vinayak, M. Yoosuf, S. C. Pradhan, T. M. Lakshmykanth, S. Soman and K. R. Gopidas, *Sustainable Energy Fuels*, 2018, **2**, 303–314.
44 M. S. Mikhailov, N. S. Gudim, E. A. Knyazeva, E. Tanaka, L. Zhang, L. V. Mikhalchenko, N. Robertson and O. A. Rakitin, *J. Photochem. Photobiol., A*, 2020, **391**, 112333.
45 P. V. Santhini, V. Jayadev, S. C. Pradhan, S. Lingamoorthy, P. R. Nitha, M. V. Chaithanya, R. K. Mishra, K. N. Narayanan Unni, J. John and S. Soman, *New J. Chem.*, 2019, **43**, 862–873.
46 A. Mishra, M. K. R. Fischer and P. Bäuerle, *Angew. Chem., Int. Ed.*, 2009, **48**, 2474–2499.
47 D. P. Hagberg, T. Edvinsson, T. Marinado, G. Boschloo, A. Hagfeldt and L. Sun, *Chem. Commun.*, 2006, 2245–2247.
48 S. M. Feldt, E. A. Gibson, E. Gabrielsson, L. Sun, G. Boschloo and A. Hagfeldt, *J. Am. Chem. Soc.*, 2010, **132**, 16714–16724.
49 D. Joly, L. Pellejà, S. Narbey, F. Oswald, T. Meyer, Y. Kervella, P. Maldivi, J. N. Clifford, E. Palomares and R. Demadrille, *Energy Environ. Sci.*, 2015, **8**, 2010–2018.
50 Y. Ren, D. Sun, Y. Cao, H. N. Tsao, Y. Yuan, S. M. Zakeeruddin, P. Wang and M. Grätzel, *J. Am. Chem. Soc.*, 2018, **140**, 2405–2408.

51 P. R. Nitha, S. Soman and J. John, *Mater. Adv.*, 2021, **2**, 6136–6168.
52 J. Zou, Q. Yan, C. Li, Y. Lu, Z. Tong and Y. Xie, *ACS Appl. Mater. Interfaces*, 2020, **12**, 57017–57024.
53 K. Zeng, W. Tang, C. Li, Y. Chen, S. Zhao, Q. Liu and Y. Xie, *J. Mater. Chem. A*, 2019, **7**, 20854–20860.
54 Z. S. Wang, N. Koumura, Y. Cui, M. Takahashi, H. Sekiguchi, A. Mori, T. Kubo, A. Furube and K. Hara, *Chem. Mater.*, 2008, **20**, 3993–4003.
55 M. J. Frisch, G. W. Trucks, H. B. Schlegel, G. E. Scuseria, M. A. Robb, J. R. Cheeseman, G. Scalmani, V. Barone, G. A. Petersson, H. Nakatsuji, X. Li, M. Caricato, A. V. Marenich, J. Bloino, B. G. Janesko, R. Gomperts, B. Mennucci, H. P. Hratchian, J. V. Ortiz, A. F. Izmaylov, J. L. Sonnenberg, Williams, F. Ding, F. Lipparini, F. Egidi, J. Goings, B. Peng, A. Petrone, T. Henderson, D. Ranasinghe, V. G. Zakrzewski, J. Gao, N. Rega, G. Zheng, W. Liang, M. Hada, M. Ehara, K. Toyota, R. Fukuda, J. Hasegawa, M. Ishida, T. Nakajima, Y. Honda, O. Kitao, H. Nakai, T. Vreven, K. Throssell, J. A. Montgomery Jr., J. E. Peralta, F. Ogliaro, M. J. Bearpark, J. J. Heyd, E. N. Brothers, K. N. Kudin, V. N. Staroverov, T. A. Keith, R. Kobayashi, J. Normand, K. Raghavachari, A. P. Rendell, J. C. Burant, S. S. Iyengar, J. Tomasi, M. Cossi, J. M. Millam, M. Klene, C. Adamo, R. Cammi, J. W. Ochterski, R. L. Martin, K. Morokuma, O. Farkas, J. B. Foresman and D. J. Fox, *Gaussian16*, 2016.
56 A. D. Becke, *J. Chem. Phys.*, 1993, **98**, 5648–5652.
57 C. Koenigsmann, T. S. Ripolles, B. J. Brennan, C. F. A. Negre, M. Koepf, A. C. Durrell, R. L. Milot, J. A. Torre, R. H. Crabtree, V. S. Batista, G. W. Brudvig, J. Bisquert and C. A. Schmuttenmaer, *Phys. Chem. Chem. Phys.*, 2014, **16**, 16629–16641.
58 P. Kumar and S. K. Pal, *Phys. Chem. Chem. Phys.*, 2016, **18**, 29571–29581.
59 P. Li, C. Song, Z. Wang, J. Li and H. Zhang, *New J. Chem.*, 2018, **42**, 12891–12899.
60 C. T. Weisspfennig, D. J. Hollman, C. Menelaou, S. D. Stranks, H. J. Joyce, M. B. Johnston, H. J. Snaith and L. M. Herz, *Adv. Funct. Mater.*, 2014, **24**, 668–677.
61 J. K. Park, J. C. Kang, S. Y. Kim, B. H. Son, J. Y. Park, S. Lee and Y. H. Ahn, *J. Phys. Chem. Lett.*, 2012, **3**, 3632–3638.
62 K. Zhu, S. R. Jang and A. J. Frank, *J. Phys. Chem. Lett.*, 2011, **2**, 1070–1076.
63 A. C. Fisher, L. M. Peter, E. A. Ponomarev, A. B. Walker and K. G. U. Wijayantha, *J. Phys. Chem. B*, 2000, **104**, 949–958.
64 P. R. F. Barnes, A. Y. Anderson, S. E. Koops, J. R. Durrant and B. C. O'Regan, *J. Phys. Chem. C*, 2009, **113**, 1126–1136.
65 J. Halme, P. Vahermaa, K. Miettunen and P. Lund, *Adv. Mater.*, 2010, **22**, E210–E234.
66 D. Cahen, G. Hodes, M. Grätzel, J. F. Guillemoles and I. Riess, *J. Phys. Chem. B*, 2000, **104**, 2053–2059.
67 F. Fabregat-Santiago, I. Mora-Seró, G. Garcia-Belmonte and J. Bisquert, *J. Phys. Chem. B*, 2003, **107**, 758–768.
68 P. S. Archana, R. Jose, M. M. Yusoff and S. Ramakrishna, *Appl. Phys. Lett.*, 2011, **98**, 2011–2014.
69 S. C. Pradhan, A. Hagfeldt and S. Soman, *J. Mater. Chem. A*, 2018, **6**, 22204–22214.
70 J. Idïgoras, G. Burdzinski, J. Karolczak, J. Kubicki, G. Oskam, J. A. Anta and M. Ziółek, *J. Phys. Chem. C*, 2015, **119**, 3931–3944.
71 J. R. Jennings, Y. Liu, Q. Wang, S. M. Zakeeruddin and M. Grätzel, *Phys. Chem. Chem. Phys.*, 2011, **13**, 6637–6648.
72 M. S. Góes, E. Joanni, E. C. Muniz, R. Savu, T. R. Habeck, P. R. Bueno and F. Fabregat-Santiago, *J. Phys. Chem. C*, 2012, **116**, 12415–12421.
73 F. Fabregat-Santiago, J. Bisquert, G. Garcia-Belmonte, G. Boschloo and A. Hagfeldt, *Sol. Energy Mater. Sol. Cells*, 2005, **87**, 117–131.
74 J. Bisquert, *J. Phys. Chem. B*, 2002, **106**, 325–333.
75 S. Soman, S. C. Pradhan, M. Yoosuf, M. V. Vinayak, S. Lingamoorthy and K. R. Gopidas, *J. Phys. Chem. C*, 2018, **122**, 14113–14127.
76 J. W. Ondersma and T. W. Hamann, *J. Phys. Chem. C*, 2010, **114**, 638–645.
77 E. M. Barea, V. Gónzalez-Pedro, T. Ripollés-Sanchis, H. P. Wu, L. L. Li, C. Y. Yeh, E. W. G. Diau and J. Bisquert, *J. Phys. Chem. C*, 2011, **115**, 10898–10902.
78 G. Boschloo and A. Hagfeldt, *Chem. Phys. Lett.*, 2003, **370**, 381–386.
79 G. Boschloo and A. Hagfeldt, *Inorg. Chim. Acta*, 2008, **361**, 729–734.
80 W. Yang, N. Vlachopoulos and G. Boschloo, *ACS Energy Lett.*, 2017, **2**, 161–167.
81 U. B. Cappel, S. M. Feldt, J. Schöneboom, A. Hagfeldt and G. Boschloo, *J. Am. Chem. Soc.*, 2010, **132**, 9096–9101.
82 M. Pazoki, A. Hagfeldt and G. Boschloo, *Electrochim. Acta*, 2015, **179**, 174–178.